Corrosion Behavior of Model Zirconium Alloys in Deaerated Supercritical Water at 500°C

Q. Peng, E. Gartner,* J.T. Busby,** A.T. Motta,*** and G.S. Was‡,*****

ABSTRACT

Several zirconium alloys with differing weight percentages of Cr, Fe, Cu, and Mo were exposed to flowing, pure supercritical water at 500°C for up to 150 days in an effort to determine their corrosion behavior for consideration in the supercritical water reactor. The weight gains of the alloys were measured, and oxides were characterized after various times. The test results showed a wide range of corrosion behavior depending on the alloy composition and process temperature. The alloys most resistant to corrosion were those containing Cr and Fe, three of which showed protective stable oxides, low corrosion rates, and no breakaway behavior. The ZrCr, ZrCu, ZrMo, and ZrCuMo alloys all exhibited high corrosion rates and non-protective oxides. Analysis of the oxide layer showed that the oxide consisted mostly of monoclinic zirconia (ZrO_2). The structure of the oxide-metal interface in the five protective alloys exhibited characteristics that were also seen in protective oxides formed at low temperature, especially the presence of a suboxide layer and an intense $(002)_T$ peak at the interface, indicating the presence of a highly oriented tetragonal phase associated with the protective oxide. The change in corrosion kinetics from cubic to linear was directly linked to the size and density of cracks in the oxides.

KEY WORDS: corrosion resistance, oxides, supercritical water, texture, zirconium alloys

INTRODUCTION

Zirconium alloys have long been used as fuel cladding in light water reactors (LWR) due to their combination of low thermal neutron absorption cross section and high resistance to waterside corrosion in the reactor environment. However, corrosion resistance becomes a limiting factor for operation in more extreme environments such as high-burnup fuel and Generation IV environments such as the supercritical water reactor (SCWR). Because a SCWR is designed to operate in a single-phase regime and with very high thermal efficiency, the peak cladding temperatures will be significantly higher than those in a LWR. The demand for the improvement of corrosion resistance has motivated both the development of new Zr alloys such as ZIRLO†,[1] and the search for a more complete understanding of the corrosion mechanism in Zr alloys.

Known influences on the corrosion resistance of Zr alloys include composition, manufacturing process (microstructure), water chemistry, temperature, irradiation, and the presence of intermetallic precipitates.[2] During the early development and testing of Zr alloys, it was discovered that traces of Cr, Fe, and Ni appeared to enhance corrosion resistance.[3-4] In Zircaloy-2 and Zircaloy-4, Fe and Cr appear primarily as small intermetallic precipitates in the alloy.[1] Observations have been made correlating the size and distribution of these particles to corrosion performance. For example, increased particle size is correlated to increased uniform corrosion resistance in pressurized water reactors (PWR),[5-6] and decreased particle size is correlated to increased nodular corrosion resistance

Submitted for publication September 2006; in revised form, February 2007.
‡ Corresponding author. E-mail: gsw@umich.edu.
* University of Michigan, Ann Arbor, MI 48109.
** Oak Ridge National Laboratory, Oak Ridge, TN 37831.
*** Penn State University, University Park, PA 16802.
**** University of Michigan, 2355 Bonisteel Blvd., 1921 Cooley Bldg., Ann Arbor, MI 48109.
† Trade name.

0010-9312/07/000099/$5.00+$0.50/0

TABLE 1
Experimental Alloys Tested

Alloy System	Alloys and Composition (wt%)	Processing Temperature
Zr-Fe-Cr	Zr-0.2Fe-0.1Cr	580°C, 720°C
	Zr-0.4Fe-0.2Cr	580°C, 720°C
Zr-Cr-Fe	Zr-0.5Cr	650°C
	Zr-0.5Cr-0.2Fe	
	Zr-1.0Cr	
	Zr-1.0Cr-0.2Fe	
Zr-Cu-Mo	Zr-0.5Cu	580°C
	Zr-0.5Cu-0.5Mo	
	Zr-1.0Cu	
	Zr-1.0Cu-0.5Mo	

in boiling water reactors (BWR).[5,7] However, there is little understanding of the mechanism by which these precipitates affect the corrosion process.

Recent investigations have also revealed that the corrosion resistance of alloys with different compositions and microstructures is related to the microstructure of the oxides formed on the alloys. For Zircaloy-4, ZIRLO, and Zr-Nb alloys exposed in 360°C water, the corrosion behavior was found to correlate with the fraction and orientation of the tetragonal zirconia (ZrO_2) formed in a very thin (<0.5 μm) layer near the oxide-metal interface.[8-10] The protective film in the most protective alloy (Zr-2.5Nb) has a greater amount of highly oriented tetragonal phase near the interface but less overall tetragonal phase in the oxide, suggesting that the formation of the interfacial tetragonal phase is correlated with the corrosion kinetics of Zr alloys.

Investigations performed to date on the corrosion of Zr alloys at high temperatures have focused on their behavior in subcritical water or steam, but not in supercritical water. The objective of this study was to investigate the performance of model Zr alloys in supercritical water to determine a technical basis for the further improvement of the Zr alloy corrosion resistance in extreme operating environments. The alloys were exposed to supercritical water for up to 150 days, and the oxides thus formed were later examined with various techniques to correlate oxide structure with corrosion behavior.

EXPERIMENTAL PROCEDURES

Alloy Preparation

Previous investigations of Zr alloys for use in superheated steam have identified materials based upon the Zr-Nb, Zr-Cr, and Zr-Cu alloy systems as being the most promising for further development.[4,11-12] In this study, a set of 30 alloys were prepared containing both solid solution alloys and precipitate-forming alloys, as described elsewhere.[13] Experiments were performed in collaboration with the Korean Atomic Energy Research Institute (KAERI, Daejeon, Korea), which was primarily responsible for testing the alloys that form extensive solid solutions, Zr-Nb and Zr-Sn, and Westinghouse Electric Co. (Monroeville, Pennsylvania), which tested the same alloys in 500°C steam. In the experiments reported here, Zr-Cr-(Fe) and Zr-Cu-(Mo) alloys were examined, as described in Table 1. The alloys can be classified into three different systems: Zr-Fe-Cr, Zr-Cr-Fe, and Zr-Cu-Mo. In addition, a specimen of stock Zircaloy-4 was tested as a reference alloy. Each of these systems contains intermetallic precipitates of varying sizes, compositions, and distributions.

Experimental alloys were prepared by arc melting as described by Jeong, et al.[13] Typical arc-melted buttons were about 70 mm in diameter and 10 mm in thickness, and weighed about 400 g. Each button was remelted at least four times to enhance chemical homogeneity. The resulting ingots were beta solution-treated at 1,050°C for 30 min in a vacuum furnace, preheated to the process temperature listed in Table 1, hot-rolled for 10 min, given an intermediate anneal, and then cold-rolled three times to a thickness of 0.8 mm. After the last rolling operation the corrosion coupons were given a final heat treatment of at least two hours at the processing temperatures indicated in Table 1. As a result of this heat treatment, all coupons were tested in the recrystallized state.

The model alloys were examined using optical and transmission electron microscopy (TEM) to ensure homogeneity of the microstructures and to establish precipitate size. The crystal structure, size, and volume fraction of the intermetallic precipitates formed in all the alloys were determined using synchrotron radiation diffraction, as described by Motta, et al.[14] The experimental alloy coupons tested in this study were 25 by 20 by 0.8 mm in size, with a drilled hole approximately 1/16 in. (1.6 mm) in diameter for hanging in the autoclave. The samples were polished with silicon carbide (SiC) paper up to 1200 grit and pickled in a solution of 10 vol% hydrofluoric acid (HF), 45 vol% nitric acid (HNO_3), and 45 vol% H_2O.

Autoclave Exposures

The corrosion tests were conducted in a flowing supercritical water loop (Figure 1). The closed loop system operated at a flow rate of 12 mL/min. Water in a main column was continually pumped through a secondary loop where impurities were filtered out by an ion exchanger. A gas line fed into the bottom of the main column, in which Ar gas was bubbled to deoxygenate the water to <10 ppb O_2.

The main loop of the system consisted of a pump, preheater, autoclave, chiller, and back-pressure regulator (BPR). Water flowed from the bottom of the main column into a high-pressure liquid chromatography pump capable of flow rates to 100 mL/min and rated

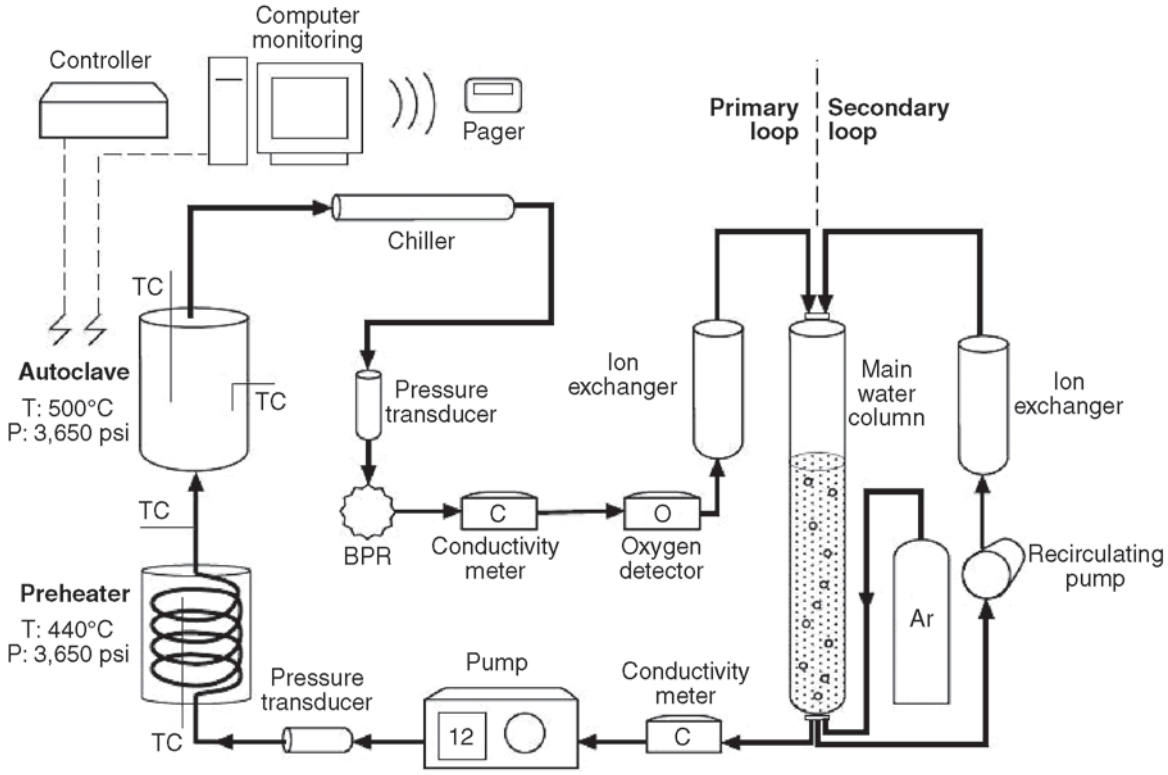

FIGURE 1. *Schematic of the flowing supercritical water loop.*

to 41.2 MPa at 24 mL/min. The water was pumped into a preheater, which raised the temperature of the water from room temperature to approximately 440°C. Water from the preheater passed through an insulated section of pipe into the autoclave (Figure 2). Water entered the autoclave at the bottom of the enclosure; the entrance of the outlet line was located at the top. As the autoclave filled, the corrosion coupons were immersed in water that was eventually forced out of the top when the autoclave was full. The autoclave was heated by three heater bands, which brought the temperature up to 500°C. They were positioned so that temperature within the autoclave remained uniform and stable. After exiting the autoclave, water passed through a chiller where heat was exchanged with an external line of flowing cold water to bring the water temperature down to room temperature. Pressure in the autoclave was controlled by a BPR rated to 27.5 MPa on the outlet line. Low-pressure water on the backside of the BPR was passed through another ion exchanger and back into the top of the main column. All high-temperature areas of the loop were enclosed in a 2.54-cm-thick Lexan† shield to protect lab personnel and equipment from any steam leaks that could occur.

Corrosion coupons were hung from an internal tree using Inconel† wire that hooked through the hole in each coupon and wrapped around a branch of the tree. The tree was capable of supporting up to 48

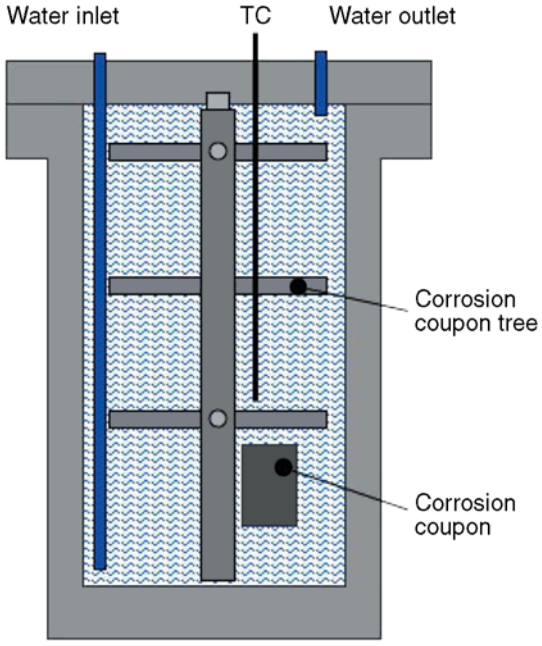

FIGURE 2. *Schematic of the autoclave used for exposure in supercritical water.*

samples at a time, allowing each sample to be exposed on all surfaces, except the small area within the hole touched by the wire. Two coupons of each alloy were tested simultaneously in all corrosion tests to increase

the reliability of the results. Coupons of the same alloy were hung on opposite sides of the autoclave to detect any lack of uniformity in internal autoclave conditions.

Conductivity, temperature, oxygen content, and pressure in the loop were measured throughout the test. Conductivity was measured in the inlet line between the main column and pump, and again in the outlet line immediately after the BPR. The ion exchange system maintained the conductivity of the inlet water at values as low as 0.06 μS/cm. The temperature was measured by thermocouples located in the center of the preheater coils, at the inlet line, attached to the external side of the autoclave, and close to the center of the inside of the autoclave. The inlet and internal thermocouples were used primarily to monitor and record the temperature of water entering and within the autoclave. The thermocouples in the preheater and on the outside of the autoclave were used by temperature controllers to control the current to the preheater and heater bands using solid-state relays. The constant feedback the controllers received from the thermocouples allowed both heating systems to be maintained at stable temperatures throughout the test, and was crucial for increasing and decreasing the temperature at system startup and shutdown. Dissolved oxygen content was measured using a high-sensitivity oxygen detector that can analyze water from either the inlet or outlet line. Two pressure transducers measured pressure at the inlet to the preheater and on the high-pressure side of the BPR. The temperature, pressure, and conductivity data were relayed to a computer running LabView† software that records new data every 10 s. To help ensure safety and system stability, LabView† can also contact lab personnel through pagers when system parameters exceed set bounds.

The tests were conducted in accordance with the standards described in ASTM G2-88.[15] Argon was bubbled through the main column until the dissolved oxygen content was less than 10 ppb. The loop was run in bypass mode until initial conductivity of the water was as low as possible, typically around 0.06 μS/cm. The autoclave was then purged with argon and filled with water. The autoclave was pressurized to approximately 25.1 MPa (3,650 psi) using the BPR and heated to 500°C. After each test ran for a specified amount of time, the autoclave temperature was lowered to room temperature and pressure, and subsequently drained and opened. Shortly after being recovered from the autoclave, the corrosion coupon surfaces were photographed with a digital camera to record their appearance.

For each alloy, two coupons were included in each exposure and weight gains were measured on both coupons. Coupons of the alloys not experiencing runaway corrosion were exposed to further corrosion tests to a total exposure time of 150 days. At 30 days, one coupon of each alloy was used for cross-sectional analysis of the oxide by removing a slice of the sample. The remaining section of the coupon was exposed in subsequent tests along with the whole companion coupon for the cross-sectional analysis at 60 days, 90 days, and 150 days, but no additional weight-gain data was obtained from the sectioned sample. Weight-gain measurements after 60 days and beyond were continued using the other coupon.

Analysis of Oxide

Weight Gain — Before the first corrosion test of an alloy, and after each subsequent test, each coupon was weighed using an analytical balance. The balance displays six significant figures for samples less than 10 g, and the standard deviation between measurements of the same mass was 0.02 mg. Because the geometry of each coupon was known, the weight gain per unit area (mg/dm^2 for this study) could be derived. Individual coupons and average weight gains for each alloy were plotted as a function of time, to determine how well corrosion rates were adhering to the expected pretransition cubic rate law. Measured weight gains were fitted to a curve of the form:

$$w = kt^n \quad (1)$$

where w is weight gain (mg/dm^2), k is the preexponential constant, t is the time of exposure (days), and n is the exponent. The parameters k and n for each coupon were determined from a power-law fit to the data at each inspection interval, and the goodness of the fit is given by the R value. Values for the two coupons of each alloy were then averaged. Alloys were also plotted against each other for comparison.

Composition — A Philips XL30† field emission gun (FEG) scanning electron microscope (SEM) equipped with x-ray energy-dispersive spectroscopy (EDS) was used to perform line scans across the cross section of the oxide at 30, 60, 90, and 150 days. The cross sections were mounted in filler resin, polished to <0.05 μm with colloidal silica, and coated with a thin layer of conductive gold. Elemental compositions were characterized with energy-dispersive analysis of x-rays (EDAX) using the Zr Lα peak at 2.042 keV and the O K peak at 0.525 keV. A minimum of 10 readings per micrometer were recorded for each line scan, and the dwell time per reading was 20 s. The EDAX software package Genesis† provided the composition in weight percent, which was then converted to atomic percent.

Thickness and Morphology — The SEM used for EDS was also used to take high-magnification images of the oxide cross section. Images in both back scatter-electron mode and secondary-electron mode were acquired. Total and sublayer oxide thickness measurements were made using micrographs at multiple points along the oxide and averaged to determine the

oxide thickness. The SEM images were also used to examine the microstructure of the oxide in high detail.

Crystal Structure — The crystal structure of the surface oxide layer of each corrosion coupon was analyzed either by using glancing-angle x-ray diffraction (XRD) (after 3, 9, and 15 days of exposure) or conventional XRD (after 150 days of exposure). Conventional XRD was used for the thicker oxide film of the 150-day coupons and provided a larger penetration depth than the glancing-angle x-ray. Both XRD techniques use a Cu $K_{\alpha 1}$ (0.1541 nm) x-ray. The glancing angle XRD uses x-rays at an angle of 3 degrees to the sample surface in a Seeman-Bohlin arrangement. Intensity data was collected using a rotating detector that traveled from 8 degrees to 40 degrees around the sample, recording intensity at each 0.05° increment. The spectrum was then matched to known peaks for ZrO_2.

Microbeam synchrotron radiation diffraction examination of the more corrosion-resistant oxide layers was performed at the Advanced Photon Source (APS) at Argonne National Laboratory (Argonne, Illinois). The beam used during the experiments was focused to 0.25 μm in the vertical direction (normal to the oxide-metal interface) and had a 2-μm footprint in the horizontal direction (parallel to the oxide-metal interface). The beam energy was 9.5 keV, corresponding to a wavelength of 0.1305 nm. Diffraction data were collected from the sample as it was translated across the beam in 0.25-μm steps using a charge-coupled device (CCD) camera. To obtain quantitative diffraction data, the digital data obtained from the two-dimensional detector were integrated over the elliptical sections for a fixed azimuthal angle, using the appropriate corrections, to obtain a plot of diffracted intensity vs two-theta angle at each location analyzed.

RESULTS AND DISCUSSION

Corrosion Behavior

In all tests, corrosion coupons of the same alloy performed similarly. Coupons of the same alloy were also similar in appearance after each corrosion test. No systematic bias in weight gain based on position within the autoclave could be detected. There was, however, considerable differences in corrosion resistance between different alloy systems and between alloys within each system, which was easily discernible even after only one day of corrosion (Table 2). The Zr-0.5Cr alloy, every alloy in the Zr-Cu-Mo system, and the control Zircaloy-4 alloy all experienced runaway (breakaway) corrosion after just one day in supercritical water at 500°C, 25.1 MPa (3,650 psi). Zr-0.5Cu-0.5Mo and Zircaloy-4 experienced the most severe corrosion, with the former alloy losing more than 1 g/dm^2 as a result of widespread spalling, and the latter alloy disintegrating. Zr-0.5Cr, Zr-0.5Cu, Zr-1.0Cu, and Zr-1.0Cu-0.5Mo grew thick, generally adherent oxides (Figure 3). The five Zr-Fe-Cr and

TABLE 2
Average Weight Gain (for Two Samples) of Tested Alloys After Exposure for 24 h

Alloy System	Alloy	Average Weight Gain 24 h (mg/dm^2)
Zr-Fe-Cr	Zr-0.2Fe-0.1Cr (720°)	27.9
	Zr-0.4Fe-0.2Cr (580°)	25.5
	Zr-0.4Fe-0.2Cr (720°)	29.5
Zr-Cr-Fe	Zr-0.5Cr	4,282.2
	Zr-0.5Cr-0.2Fe	32.0
	Zr-1.0Cr-0.2Fe	38.0
Zr-Cu-Mo	Zr-0.5Cu	3,966.5
	Zr-0.5Cu-0.5Mo	−1,669.2 (spalling)
	Zr-1.0Cu	550.3
	Zr-1.0Cu-0.5Mo	576
Reference	Zircaloy-4	Disintegrated

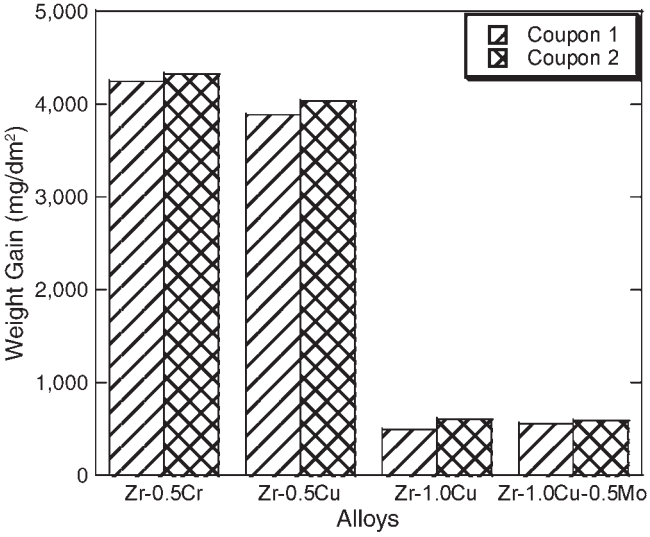

FIGURE 3. *Weight gains of alloys with poor corrosion resistance after a 24-h exposure in 500°C, deaerated SCW.*

Zr-Cr-Fe alloys exhibited much greater corrosion resistance after one day, with no coupons exceeding a weight gain of 40 mg/dm^2 (Figure 4). It is worth noting that these results are consistent with tests conducted on the same alloys by KAERI in a static system and by Westinghouse at 500°C in steam.[14]

Five alloys were identified as corrosion-resistant and were subjected to longer tests. All corrosion coupons of the five alloys remained intact through 150 days of exposure (Table 3). Of this group, Zr-1.0Cr-0.2Fe had the thickest adherent oxide weight gain over this period. The Zr-0.4Fe-0.2Cr alloy processed at 580°C exhibited the least weight gain over the course of the experiment. Both of these results were consistent with the average weight gain of the respective alloys after one day. Two of the alloys, (Zr-0.4Fe-0.2Cr [H] and Zr-1.0Cr-0.2Fe) exhibited a tran-

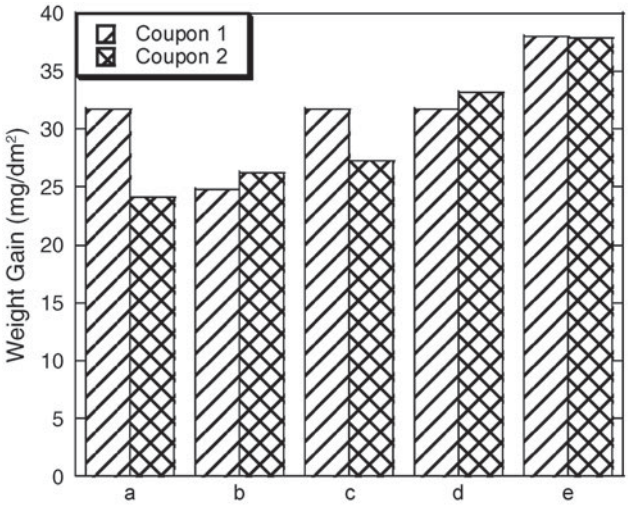

FIGURE 4. *Weight gains of alloys surviving beyond 24 h in 500°C, deaerated SCW: (a) Zr-0.2Fe-0.1Cr (H), (b) Zr-0.4Fe-0.2Cr (L), (c) Zr-0.4Fe-0.2Cr (H), (d) Zr-0.5Cr-0.2Fe, and (e) Zr-1.0Cr-0.2Fe.*

sition in corrosion kinetics, with the rate becoming linear at about 60 days of exposure. A plot of weight gain for the five alloys over 150 days of exposure is shown in Figure 5.

The rate constants obtained from a power law fit of the weight-gain kinetics shown in Figure 5 are given in Table 4. These values were updated after each exposure period for alloys Zr-0.2Fe-0.1Cr, Zr-0.4Fe-0.2Cr (L), and Zr-0.5Cr-0.2Fe. For alloys Zr-0.4Fe-0.2Cr (H) and Zr-1.0Cr-0.2Fe, the rate constants after the exposure time of 60 days are not given in the table, since as shown in Figure 5, the oxidation behavior of these two alloys became nearly linear after 60 days of exposure. During the 150 days of exposure, the value of n stayed in the range from 0.35 to 0.38, and the R^2 of the fit was within 0.014 of 1.0, indicative of roughly cubic kinetics. The exponents for alloys Zr-0.4Fe-0.2Cr (H) and Zr-1.0Cr-0.2Fe up through 60 days were also within this range. These exponents were in very good agreement with those observed in the static autoclave and in steam experiments.[14]

Oxide Characterization

Cross-sectional analysis of the coupons after 30, 60, 90, and 150 days of exposure performed using SEM are shown in Figures 6(a) through (d). As can be seen, changes of the thickness of the oxide film at each exposure period were consistent with the increasing weight gains for all alloys. The thickness of the oxide film was quite uniform for alloys Zr-0.2Fe-0.1Cr, Zr-0.4Fe-0.2Cr (L), Zr-0.4Fe-0.2Cr (H), and Zr-0.5Cr-0.2Fe. However, alloy Zr-1.0Cr-0.2Fe exhibited variations of the film thickness on the order of ±2 μm. In addition, an inner transition layer below the oxide film was found for all alloys. The inner transition layer had a smoother, lighter appearance than the rest of the metal and was therefore measured directly from the micrographs. This inner transition layer was interpreted as being the region in the metal that contained a large amount of dissolved oxygen that diffused ahead of the oxide front as previously seen during corrosion testing of other Zr alloys.[8-9]

Measurements of oxide thickness after 150 days of exposure are given in Table 5. The first column shows the calculated thickness by dividing the weight gain using the equality 1 μm = 14.8 mg/dm^2. The two following columns show the actual metallography measurements, both of the oxide itself and of the inner layer. It is clear that the measured and calculated results do not agree, because not all oxygen is being used to form ZrO_2, but is also used to form the inner layer. The inner transition (suboxide) layer has been identified previously as containing about 30 at% oxygen,[9] so the weight gain can be approximated as:

$$w = 14.8 \times \delta_{ZrO_2} + \left(\frac{0.3}{0.66}\right) \times 14.8 \times \delta_{suboxide} \qquad (2)$$

TABLE 3
Weight Gain of Alloys for Exposures Up to 150 Days

	Weight Gain (mg/dm^2)											
Alloy/Coupon Number	**Day 1**	**2**	**3**	**6**	**9**	**15**	**21**	**30**	**60**	**90**	**120**	**150**
Alloy Zr-0.2Fe-0.1Cr (H)/1221	31.7	—	46.9	57.7	65.0	77.8	86.5	98.1	130.3	157.4	181.8	210.7
Alloy Zr-0.4Fe-0.2Cr (L)/1322	26.2	—	42.3	51.7	59.4	73.2	81.1	91.8	118.1	144.6	163.6	183.5
Alloy Zr-0.4Fe-0.2Cr (H)/1421	31.7	—	48.8	60.6	68.8	84.4	94.4	108.0	146.1	197.8	242.7	305.8
Alloy Zr-0.5Cr-0.2Fe/ 2222	33.2	42.9	47.1	58.1	66.1	78.8	88.2	100.5	125.2	157.9	179.8	204.1
Alloy Zr-1.0Cr-0.2Fe/ 2421	38.1	47.2	53.8	64.8	73.8	91.1	105.6	122.9	168.1	260.8	341.6	422.7

where δ_{ZrO_2} is the oxide thickness and $\delta_{suboxide}$ is the suboxide layer thickness. Using Equation (2) we calculate an effective thickness, which can be compared to the weight gain (last column of Table 5). We obtain reasonable agreement with the measured weight-gain values (compare first and last columns), especially considering that both the oxide layer and suboxide layer thicknesses vary laterally along the oxide-metal interface. Note that the observed "suboxide" or transition region is much thicker in these samples exposed to high temperatures (3 μm to 7 μm) than in samples tested at lower temperatures in which this transition layer thickness was observed to be approximately 0.1 μm to 0.5 μm.[8] While a complete analysis of the suboxide layer thickness was conducted only after 150 days of exposure, the data confirm that the suboxide/total oxide thickness ratio increases with the protectiveness of the film.

Observations of the oxide film by SEM also revealed a noticeable amount of lateral cracks in the film. The alloys Zr-0.4Fe-0.2Cr (H) and Zr-1.0Cr-0.2Fe, which exhibited more weight gain than other alloys, had the highest density and largest size of lateral cracks in the oxide following each exposure period. In addition, these two alloys showed a significant increase in the density of the cracks in the oxide film at the onset of the kinetic transition (after 60 days of exposure) when the corrosion rate increased and the kinetics became linear. The cracks in the oxide films of all coupons were generally parallel to the surface of the coupon, as normally observed, and in agreement with the presence of in-plane compressive stresses arising from the imperfect accommodation of volume expansion upon oxidation. The kinetic transition is

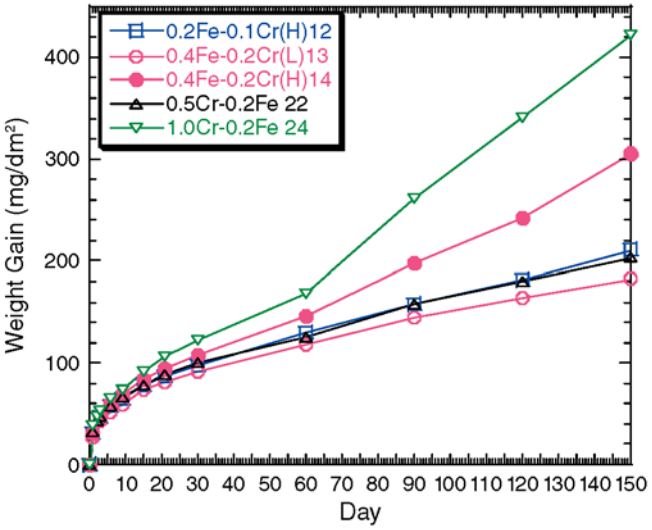

FIGURE 5. *Weight gains of the five surviving alloys through 150 days of exposure in 500°C, deaerated SCW.*

TABLE 4

Rate Constants of Surviving Experimental Alloys Through 150 Days

Alloy/Coupon Number	Day 3			Day 6			Day 9			Day 15			Day 21		
	k	n	R^2	k	n	R^2	k	n	R^2	k	n	R^2	k	n	R^2
Alloy Zr-0.2Fe-0.1Cr (H)/1221	31.70	0.357	1	31.90	0.336	0.9974	32.05	0.327	0.9976	32.04	0.327	0.9986	32.07	0.327	0.9992
Alloy Zr-0.4Fe-0.2Cr (L)/1322	26.20	0.436	1	26.62	0.384	0.9866	26.81	0.370	0.9914	26.81	0.371	0.9956	26.92	0.366	0.9968
Alloy Zr-0.4Fe-0.2Cr (H)/1421	31.70	0.393	1	31.98	0.364	0.9956	32.17	0.353	0.9962	32.11	0.355	0.9976	32.13	0.355	0.9986
Alloy Zr-0.5Cr-0.2Fe/2222	33.49	0.324	0.9851	33.71	0.308	0.9944	33.74	0.307	0.9974	33.62	0.311	0.9980	32.53	0.315	0.9984
Alloy Zr-1.0Cr-0.2Fe/2421	38.07	0.314	0.9998	38.33	0.298	0.9980	38.32	0.298	0.9990	37.88	0.313	0.9938	37.41	0.327	0.9912

Day 30			Day 60			Day 90			Day 120			Day 150		
k	n	R^2	k	n	R^2	k	n	R^2	k	n	R^2	k	n	R^2
32.03	0.328	0.9994	31.61	0.337	0.9960	31.07	0.347	0.9934	30.55	0.357	0.9916	29.93	0.369	0.9868
27.02	0.363	0.9978	27.09	0.361	0.9988	26.84	0.367	0.9968	26.62	0.372	0.9966	26.36	0.377	0.9956
32.09	0.356	0.9990	31.68	0.364	0.9964	—	—	—	—	—	—	—	—	—
33.38	0.319	0.9982	33.28	0.321	0.9990	32.17	0.338	0.9908	32.204	0.343	0.9894	31.71	0.352	0.9874
36.95	0.339	0.9906	36.11	0.356	0.9880	—	—	—	—	—	—	—	—	—

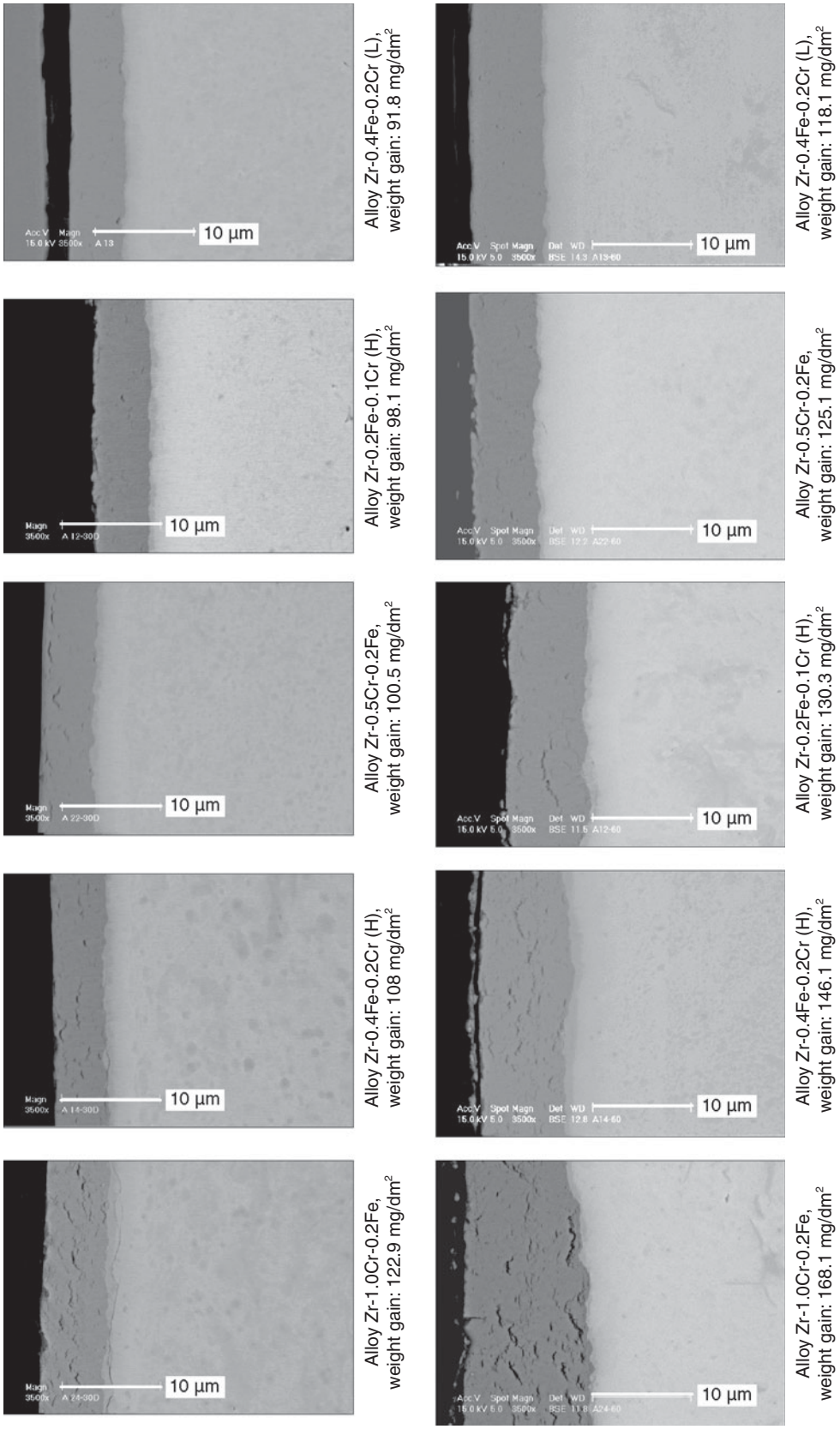

FIGURE 6 (continued on next page). *Cross-sectional images of the coupons and their weight gains following (a) 30 days, (b) 60 days, (c) 90 days, and (d) 150 days of exposure in deaerated SCW at 500°C.*

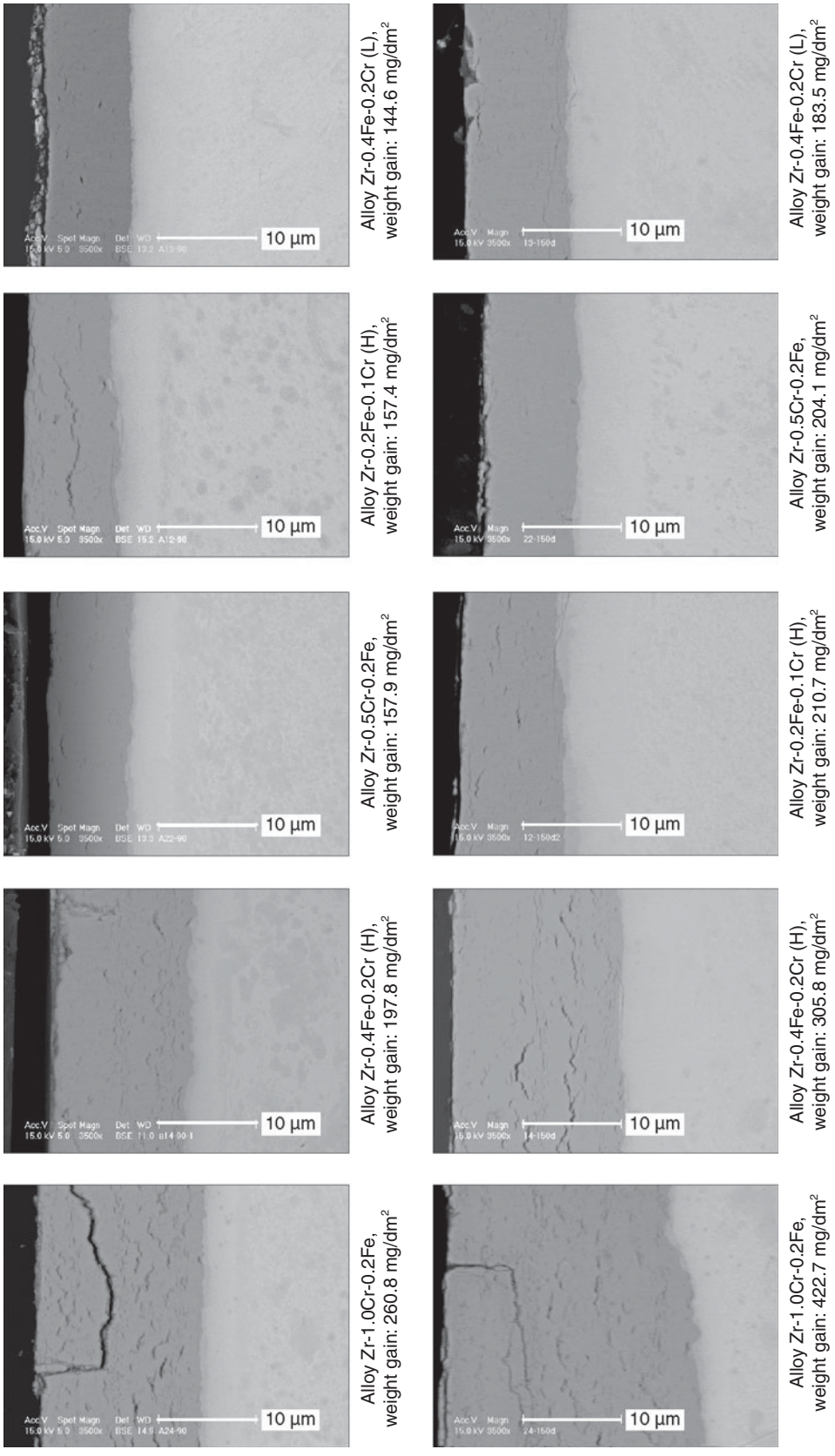

FIGURE 6 (continued). *Cross-sectional images of the coupons and their weight gains following (a) 30 days, (b) 60 days, (c) 90 days, and (d) 150 days of exposure in deaerated SCW at 500°C.*

TABLE 5
Measured and Calculated Oxide Thickness After 150 Days

Alloy/Coupon Number	Oxide Thickness Calculated from Weight Gain (μm)	Measured Suboxide Layer (μm)	Measured Oxide Layer (μm)	Calculated Equivalent Thickness from Equation (2) (μm)
Alloy Zr-0.2Fe-0.1 Cr (H)/1221	14.24	6.17	10.74	14.48
Alloy Zr-0.4Fe-0.2Cr (L)/1322	12.40	6.02	9.60	13.25
Alloy Zr-0.4Fe-0.2Cr (H)/1421	20.66	4.27	21.70	24.29
Alloy Zr-0.5Cr-0.2Fe/2222	13.79	7.85	9.51	14.27
Alloy Zr-1.0Cr-0.2Fe/2421	28.56	3.03	25.39	27.23

normally associated with a loss of protectiveness in the oxide layer allowing the formation of short-circuit paths that accelerate the transport of the oxidizing species through the oxide. The marked increase in crack density observed at the transition can be connected with the transition if a small amount of vertical cracks or small pores are also present to create a percolation path for the oxidizing species to reach the oxide-metal interface.[10] Although it is always difficult to distinguish cracks created during the experimentation from those caused by sample preparation, a few large cracks vertical to the coupon surface were found in the oxide on alloy Zr-1.0Cr-0.2Fe, in agreement with the above scheme.

Figures 7 and 8 show the composition of the oxide film following 30, 60, 90, and 150 days of exposure measured by line scans for alloys Zr-0.4Fe-0.2Cr (L) and Zr-0.4Fe-0.2Cr (H), respectively. These two alloys were selected because among the five alloy conditions they exhibit the largest disparity in corrosion behavior. The results indicate that the atomic percent of Zr and O in the oxide film are similar for both alloys, and close to that of ZrO_2.

Figure 9 shows XRD spectra obtained using both glancing-angle and normal incidence for various oxide thicknesses. Metal peaks are visible in the thinner oxide samples, which disappear in the thicker oxides. Examination of the XRD spectra revealed that the dominant phase present on the oxide surface is monoclinic ZrO_2 for all experimental alloys over the course of the experiment, as seen by many researchers. The indexed spectrum was a close match to a specimen of pure monoclinic ZrO_2, except that the relative intensity of some peaks were different from that obtained in powder diffraction, due to preferred orientation (texture) in the oxide film. Previous observations of the oxide texture in Zr alloys[16] have indicated the development of a texture in which the monoclinic oxide growth direction is between $[\bar{2}01]_M$ and $[\bar{4}01]_M$. This oxide growth direction is close to that which has been predicted by Li, et al.,[16] to minimize the accumulated stresses in the growing oxide. The observed texture is in agreement with these values, since the intensity of the $(\bar{4}01)_M$ peak is much higher than would be seen in a random powder pattern (this is a 4% peak in a random power pattern); the intensity of the $(200)_M$ peak is comparable to that of the 100% peak $(\bar{1}11)_M$ peak, etc. It is interesting to note that the monoclinic oxide texture of the oxide film changes with overall oxide thickness, with the growth direction becoming more closely aligned with $[\bar{4}01]_M$, as evidenced by the growing intensity of this peak relative to the 100% intensity peak in the power diffraction file, the $(\bar{1}11)_M$ peak.

These oxides were also examined using microbeam synchrotron radiation diffraction at the Advanced Photon Source. An example of the results obtained is shown in the 3D plot depicted in Figure 10.[14] The diffracted intensity vs. two-theta angle is plotted for each location in the metal and in the oxide, from 3 μm into the metal up to 4 μm into the oxide. The metal peaks disappear at the oxide-metal interface and are substituted by the monoclinic and tetragonal oxide peaks. The intensity of the tetragonal peaks in the bulk of the oxide is low—only the $(101)_T$ peak is seen and its intensity is much lower than that of the monoclinic peaks. Suboxide peaks (marked S) are seen as shoulders of the alpha Zr peaks and they extend a few micrometers into the metal, in agreement with the thicknesses estimated from SEM. In this orientation (cross section) the most intense monoclinic peak in the oxide is the $(\bar{1}11)_M$ peak at 26.58 degrees two-theta for the wavelength we used (9.5 keV). This also means that the $(200)_M$ peak intensity should be very low, since that peak is aligned close to (within 10 degrees to 15 degrees) the oxide growth direction, and this is verified.

The most remarkable feature of the diffraction pattern sequence shown in Figure 10 is the peak labeled $[002]_T$, the intensity of which is very high in the 0.5-μm region right ahead of the oxide-metal interface. This peak is normally observed in the same location—just ahead of the newly formed oxide at the oxide-metal interface—in oxides that exhibit protective behavior during low-temperature corrosion testing (but at much lower intensities).[10] This peak was seen, with similar intensities as in Figure 10, in the oxides formed in all of the five protective alloys that were tested in the 150 days of this study. The peak was also seen in oxides formed in Zr-Nb alloys under supercritical water conditions.[14] Preliminary results

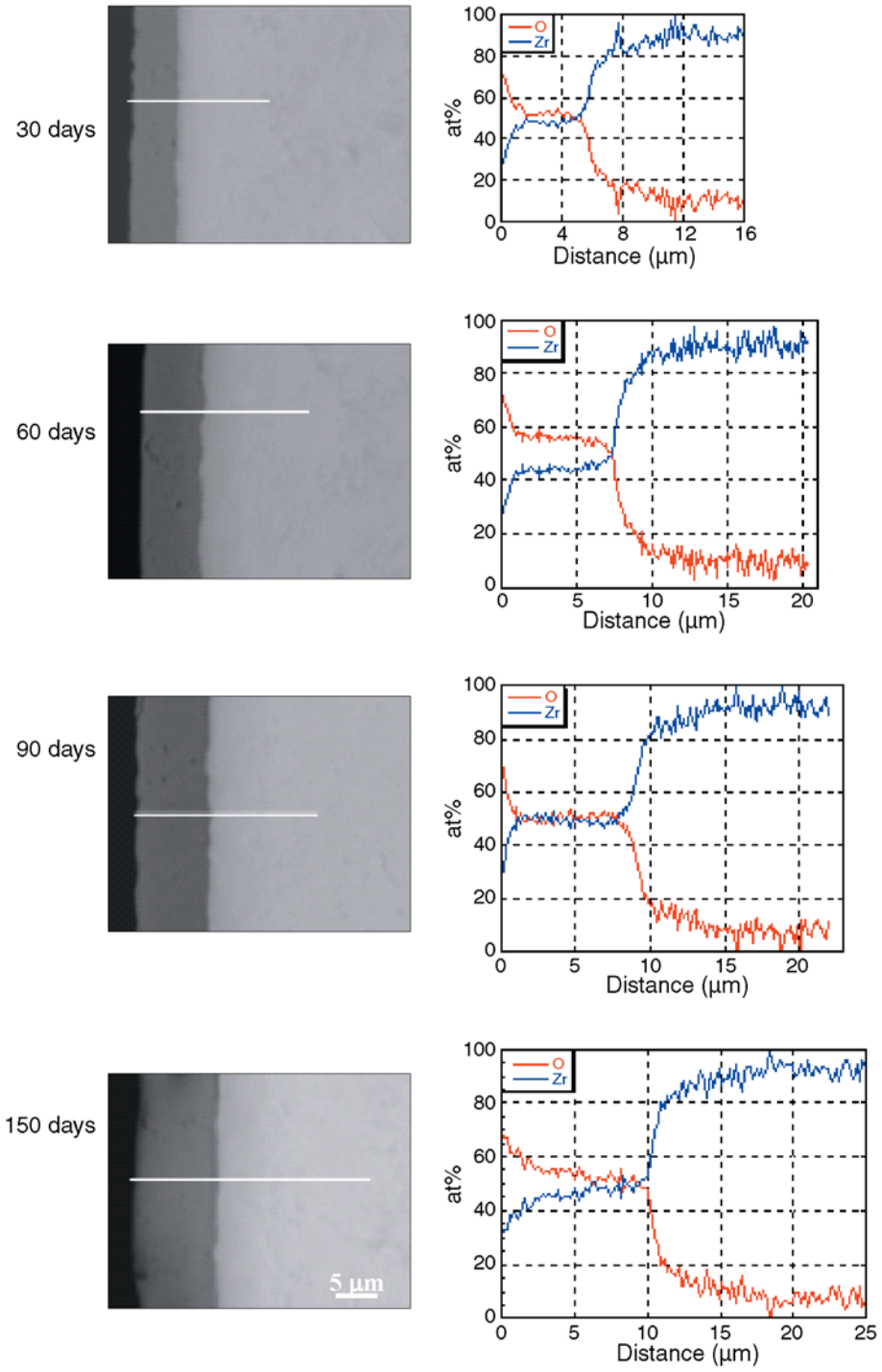

FIGURE 7. *Results of the SEM-EDS scan for alloy Zr-0.4Fe-0.2Cr (L) after exposure to 500°C, deaerated SCW.*

show that this peak is present in those oxides that exhibit protective behavior (similarly to the low-temperature behavior) and is absent in oxides that are nonprotective and that exhibit high corrosion rates.

The presence of this peak at the oxide-metal interface has been interpreted in the low-temperature results as originating from the presence of a highly oriented tetragonal phase that has an epitaxial relationship with the matrix, $002_T//020_M$. This phase leads to a correctly oriented monoclinic phase for stress minimization, which, in turn, leads to an oxide layer that will stay intact longer. Thus, the presence of this phase and its subsequent transformation to the monoclinic phase may induce the formation of a protective monoclinic oxide, as observed. The similarity of the oxide structures at the oxide-metal interface

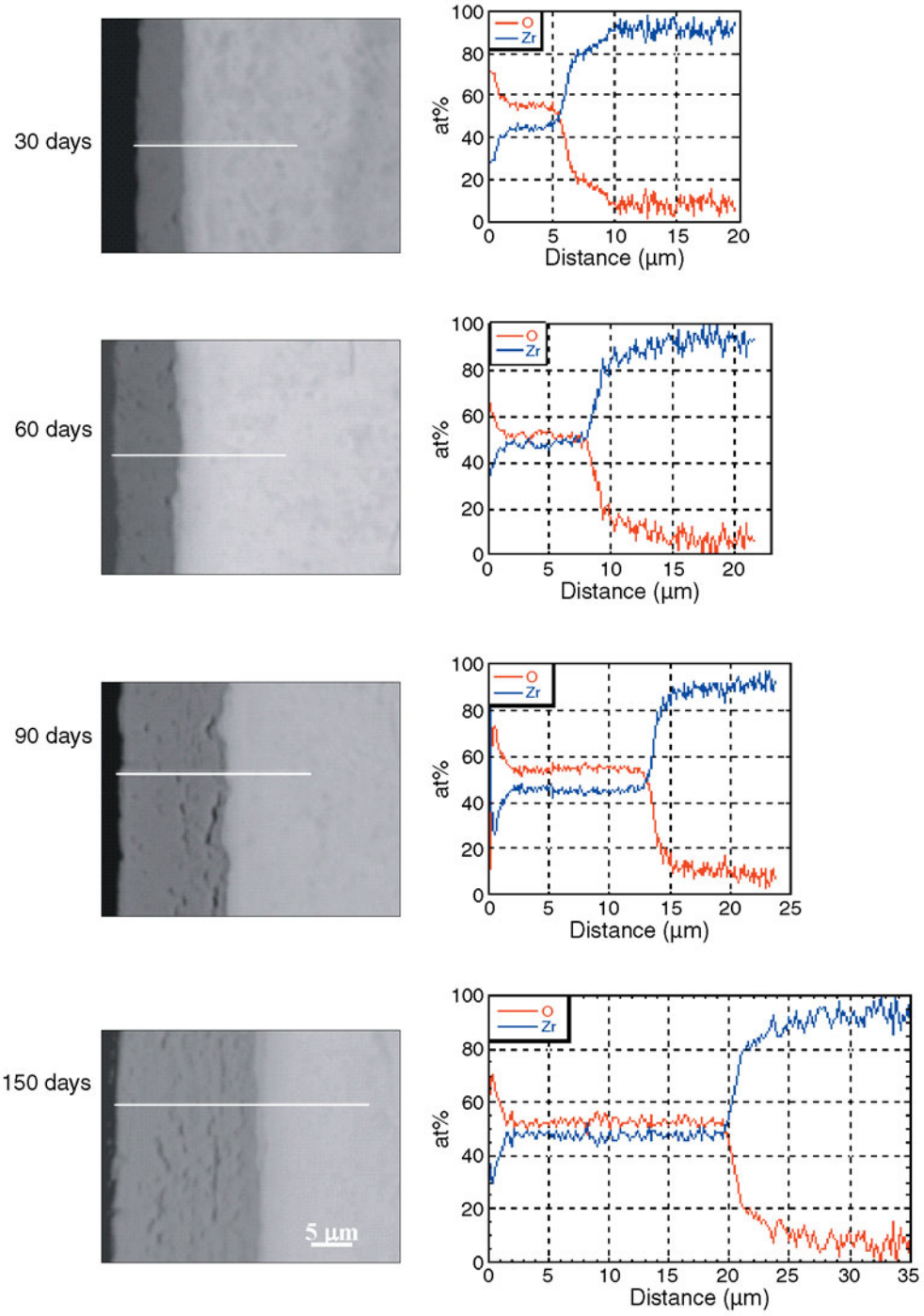

FIGURE 8. *Results of the SEM-EDS scan for alloy Zr-0.4Fe-0.2Cr (H) after exposure to 500°C, deaerated SCW.*

appears to indicate that the same oxide protection mechanisms are operative at 360°C and at 500°C. The higher corrosion rates at 500°C compared to 360°C likely account for the thicker suboxide formed and for the higher intensity of tetragonal phase at the interface.

It is clear that this protection mechanism is linked to the alloy microchemistry and microstructure. However, the mechanistic connection between the structure of the alloy and that of the protective oxide is still unclear and warrants further investigation.

CONCLUSIONS

❖ A set of model Zr alloys was tested in flowing supercritical water at 500°C for up to 150 days, and the resulting oxide layers compared and contrasted to the corrosion behavior.

❖ A wide range of corrosion behavior was observed, depending on the alloy. The best alloys were from the Zr-Fe-Cr system that exhibited protective behavior for the full 150 days of the test.
❖ Corrosion of alloys Zr-0.5Cr, Zr-Cu-Mo, and the control Zircaloy-4 alloy was extensive even after 1 day of exposure in deaerated supercritical water at 500°C. The corrosion resistance of these alloys was much inferior to that of the five Zr-Fe-Cr and Zr-Cr-Fe alloys, which survived for 150 days of exposure, with relatively low corrosion.
❖ The relative corrosion resistance of the five surviving alloys remained consistent over the entire exposure period. The oxides grew with roughly cubic weight gain kinetics over the entire 150-day exposure period for alloys Zr-0.2Fe-0.1Cr (H), Zr-0.4Fe-0.2Cr (L), and Zr-0.5Cr-0.2Fe, and over 60 days for alloys Zr-0.4Fe-0.2Cr (H) and Zr-1.0Cr-0.2Fe. These last two alloys exhibited roughly linear corrosion after about 60 days of exposure.
❖ The change of the thickness of the oxide film at each exposure period was consistent with the weight gain for the five surviving alloys. These oxides exhibited cracks in the film, the amount and size of which increased monotonically with oxide thickness. Oxides were characterized by a thick outer layer in which the atomic percent of Zr and O were close to that of ZrO_2, and a thinner inner transition layer that was deficient in oxygen, identified with the suboxide layer.
❖ The texture of the oxides was consistent with the oxide growth textures normally observed during low-temperature corrosion. The structure of the oxide-metal interface in the five protective alloys exhibited characteristics that were also seen in protective oxides formed at low temperature, especially the presence of a suboxide layer and of a large $(002)_T$ peak at the interface, indicating the presence of a highly oriented tetragonal phase, which helps form the protective oxide. This suggests that the mechanisms of corrosion protection by alloying elements are similar at high and low temperatures.

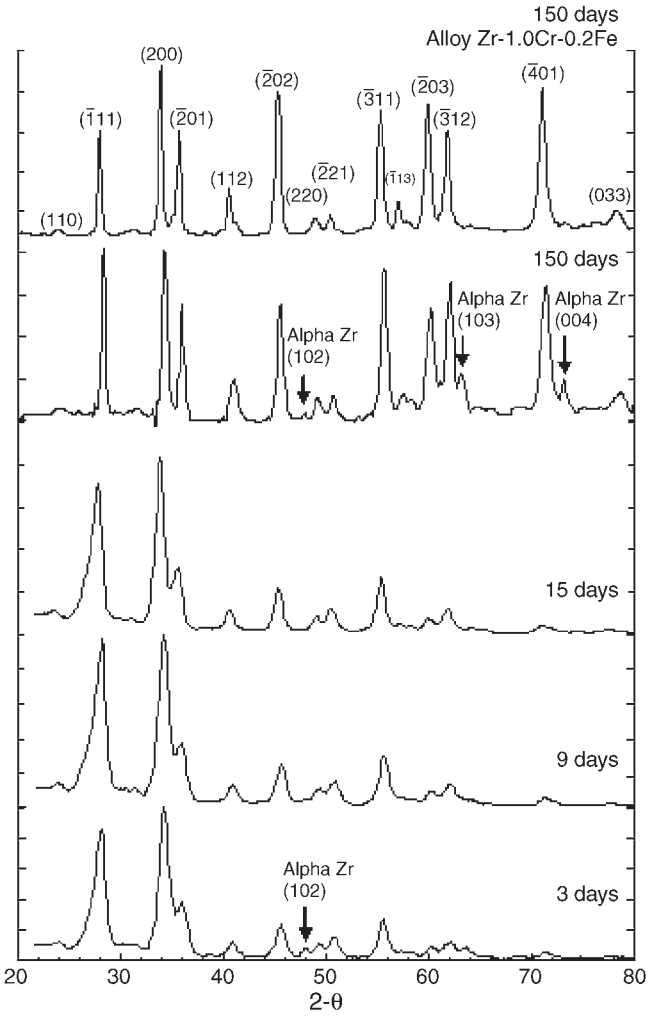

FIGURE 9. *XRD spectra of alloy Zr-0.4Fe-0.2Cr (L) oxide at 3, 9, 15, and 150 days and alloy Zr-1.0Cr-0.2Fe oxide at 150 days in deaerated, 500°C SCW. All other experimental alloys had similar spectra.*

ACKNOWLEDGMENTS

The authors acknowledge the help of M. Atzmon in the acquisition of glancing-angle x-ray data and the High-Temperature Corrosion Laboratory at the University of Michigan for the supercritical water facilities. This research was supported by a Department of Energy, International Nuclear Energy Research Initiative (DOE INERI) grant no. DE-FG07-03RL14530. Use of the Advanced Photon Source was supported by the U.S. Department of Energy, Basic Energy Sciences, Office of Science, under contract no. W-31-109-Eng-38.

REFERENCES

1. G.P. Sabol, G.R. Kilp, M.G. Balfour, E. Roberts, "Development of a Cladding Alloy for High Burnup," 8th Int. Symp. on Zirconium in the Nuclear Industry, vol. STP 1023 (West Conshohocken, PA: ASTM International, 1989), p. 227-244.
2. "Waterside Corrosion of Zirconium Alloys in Nuclear Power Plants," International Atomic Energy Agency, Vienna, Austria, TECDOC-996, 1998.
3. S. Kass, "The Development of the Zircaloys," Symp. on Corrosion of Zirconium Alloys, vol. STP 368 (West Conshohocken, PA: ASTM International, 1964), p. 3-27.
4. B. Cox, "The Effects of Some Alloying Additions on the Oxidation of Zirconium in Steam," U.K. Report, AERE-R4458, U.K. Atomic Energy Authority, Harwell, 1963.
5. F. Garzarolli, H. Stehle, "Behavior of Core Structural Materials in Light Water Cooled Power Reactors," in IAEA Symp. on Improvements in Water Reactor Fuel Technology and Utilization, IAEA SM 288/24 (Vienna, Austria: International Atomic Energy Agency, 1987), p. 387-407.
6. F. Garzarolli, R. Holzer, Nucl. Energy (J. Br. Nucl. Energy Soc.) 31 (1992): p. 65.
7. F. Garzarolli, W. Goll, A. Seibold, I. Ray, "Effect of In-PWR Irradiation on Size, Structure, and Composition of Intermetallic Precipitates of Zr Alloys," in Zirconium in the Nuclear Industry: 11th Int. Symp., STP 1295 (West Conshohocken, PA: ASTM International, 1996), p. 541-556.
8. A. Yilmazbayhan, A.T. Motta , R.J. Comstock, G.P. Sabol, J. Nucl. Mater. 324 (2004): p. 6-22.
9. A. Yilmazbayhan, E. Breval, A. Motta, R. Comstock, J. Nucl. Mater. 349 (2006): p. 265-281.

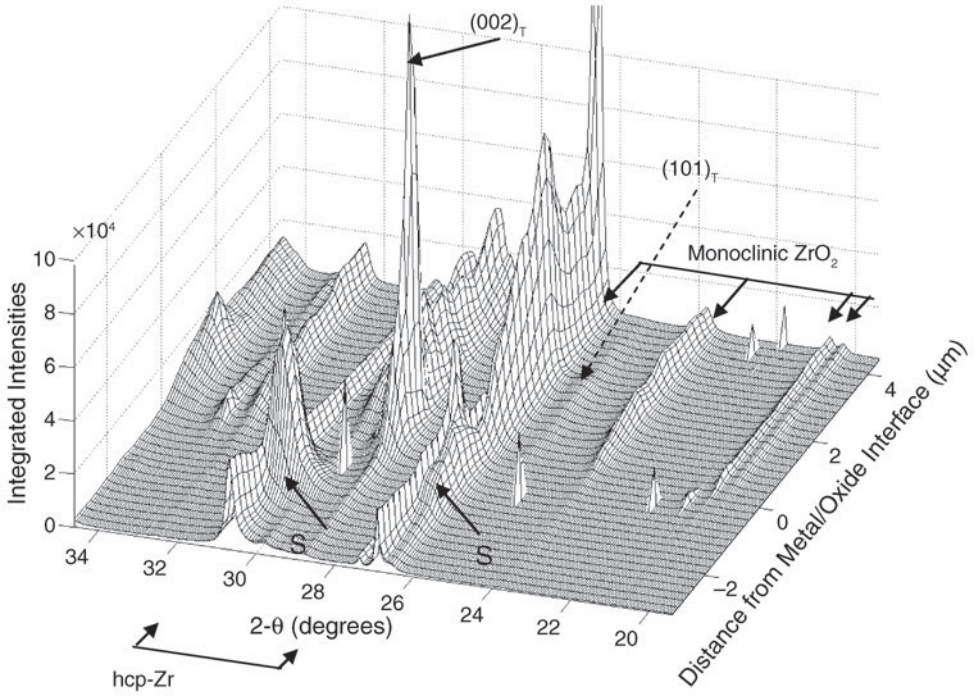

FIGURE 10. *Diffracted intensity (in arbitrary units) vs. two-theta diffraction angle as a function of position in the oxide layer for alloy Zr-1.0Cr-0.2Fe, after exposure to 500°C supercritical water for 150 days to a total weight gain 422.7 mg/dm², which corresponds to an oxide thickness of about 20 μm.*[14]

10. A.T. Motta, A. Yilmazbayhan, R.J. Comstock, J. Partezana, G.P. Sabol, Z. Cai, B. Lai, J. ASTM Int. 2, (2005), paper no. JAI 12375.
11. D. Weinstein, F.C. Holtz, "Development of Improved Zirconium Alloys for Use in Supercritical Water and Steam," in Proc. USAEC Symp. on Zirconium Alloy Developement, held Nov. 12-14, GEAP-4089, vol. 1 (Castlewood, Pleasanton, CA: 1962), paper no. 6.
12. H.H. Klepfer, D.L. Douglass, "Factors Limiting the Use of Zirconium Alloys in Superheated Steam," ASTM STP 368 (West Conshohocken, PA: ASTM International, 1964), p. 118.
13. Y.H. Jeong, J.Y. Park, H.G. Kim, J.T. Busby, E.L. Gartner, M. Atzmon, G.S. Was, R.J. Comstock, M. Gomes da Silva, A.T. Motta, "Corrosion of Zirconium-Based Fuel Cladding Alloys in Supercritical Water," Proc. 12th Int. Conf. on Environmental Degradation of Materials in Nuclear Power Systems–Water Reactors, eds. T. Allen, P.J. King, L. Nelson (Warrendale, PA: The Minerals, Metals, and Materials Society [TMS], 2005), p. 1,369-1,377.
14. A.T. Motta, A. Yilmazbayhan, M. Gomes da Silva, R.J. Comstock, G.S. Was, J.T. Busby, E. Gartner, Q. Peng, Y.H. Jeong, J.Y. Park, J. Nucl. Mater. (2006), in press.
15. ASTM G2-88(2002), "Standard Test Method for Corrosion Testing of Products of Zirconium, Hafnium, and Their Alloys in Water at 680°F or in Steam at 750°F," in Annual Book of ASTM Standards (West Conshohocken, PA: ASTM International, 2002).
16. H. Li, H.M. Glavicic, J.A. Spuznar, Mater. Sci. Eng. A366 (2004): p. 164-174.

Conference of Metallurgists Issues Call for Papers

The Conference of Metallurgists (COM2008), the annual conference of the Metallurgical Society of the Canadian Institute of Mining, Metallurgy, and Petroleum, has issued a call for papers for the event scheduled to take place in Winnipeg, Manitoba, Canada, August 24-27, 2008.

The conference will cover the following topics:

—Zinc and lead metallurgy
—Aerospace materials
—Water, air, and land issues
—Corrosion and wear of materials
—Lightweight automotive
—Management in metallurgy
—Advanced characterization
—Functional nanomaterials

Prospective authors are invited to submit 100-word abstracts online at http://www.cim.org/COM2008/ no later than December 31, 2007. Abstracts should include the title, author(s) name, affiliation, mailing address, phone number, and e-mail address.

Authors will be notified regarding acceptance by January 15, 2008. Camera-ready papers are due no later than March 31, 2008.

For more detailed information, please contact the technical program chair, William Caley, Dalhousie University, Halifax, Nova Scotia, Canada; phone: 902/494-3298; e-mail: william.caley@dal.ca; Web site: http://www.metsoc.org/com2008/.